

Robust Thermophysics-based Interpretation of Radiometrically Uncalibrated IR Images for ATR and Site Change Detection

N. Nandhakumar[†], J. Michel[†], D.G. Arnold^{‡†}, G. Tsihrintzis[†], V. Velten[‡]

[†] Dept of Electrical Engineering, Univ. of Virginia, Charlottesville, VA 22903

[‡] Wright Laboratory - WL/AARA, Wright Patterson Air Force Base, OH 45433-7001

The authors may be reached at {nandhu, michel, dga3n, gat6v}@Virginia.edu, vvelten@mbvlab.wpafb.af.mil

This research was supported by a RADIUS seed contract from Lockheed-Martin, AFOSR contract F49620-93-C-0063, the AFOSR grant LRIR-93WL001, an AFOSR Laboratory Graduate Fellowship, and ARPA contract F33615-94-C-1529.

Abstract

We recently formulated a new approach for computing invariant features from infrared (IR) images. That approach is unique in the field since it considers not just surface reflection and surface geometry in the specification of invariant features, but it also takes into account internal object composition and thermal state which affect images sensed in the non-visible spectrum. In this paper we extend the thermophysical algebraic invariance (TAI) formulation for the interpretation of uncalibrated infrared imagery, and further reduce the information that is required to be known about the environment. Features are defined such that they are functions of only the thermophysical properties of the imaged objects. In addition, we show that the distribution of the TAI features can be accurately modeled by symmetric alpha-stable models. This approach is shown to yield robust classifier performance. Results on ground truth data and real infrared imagery are presented. The application of this scheme for site change detection is discussed.

Keywords

Object Recognition, Feature Invariance, Alpha-Stable Distributions, Infrared Image Analysis, Physics-based Computer Vision

I. INTRODUCTION

Object recognition requires robust and stable features that are separable in feature space. An important characteristic of these features is that they be invariant to scene conditions, such as illumination, and changes in viewpoint/object pose. The formulation of invariant features, and the quantitative analysis of feature variance is currently being addressed by a number of researchers in the computer vision community, and has led to the establishment of a mature and growing theory of feature invariance. Such efforts have primarily considered reflected-light imagery – formed by sensing visible wavelength energy. This investigation has resulted in a number of distinct (yet related) approaches that may be loosely grouped into three categories: (1) Geometric Invariance (GI), (2) Quasi-Invariance (QI), and (3) Intensity-based Invariance (II).

Geometric invariants have been investigated since the inception of the field of image analysis in the early 1960s (actually, such investigation can be traced back to the onset of photogrammetry in the 19th century). The main issue is the investigation of features that are invariant with respect to changes in viewpoint. Geometric invariants come in two basic “flavors”, algebraic and differential. Algebraic invariants are based on the global configu-

ration of features extracted from an object, and involve the notion of algebraic shapes, e.g., shapes are analytically expressed as 2D conics, and invariant relationships are identified between conics belonging to an object. Differential invariants are polynomial expressions involving the local curvature properties of 2D and 3D curves and are computed for each point on the curve. Thus differential invariants are actually parameter space “signatures” (e.g., a locus of point in an abstract parameter space) that are unique to the object, so that differences between two parameter space signatures define different objects. A close relationship (an equivalence in some cases) has been shown between some formulations of differential invariants and algebraic invariants [1]. There are several examples of geometric (actually algebraic) invariants of planar configurations under projective transformation, such as the cross ratio using 4 collinear points, 5 coplanar points with no three being collinear, a conic and two non-tangent lines, and a pair of coplanar conics. Many new geometric invariants have been researched in recent work [2] - [10].

Quasi-Invariance (QI) can be thought of as a relaxation of the central notion of GI [11], [12]. A Quasi-Invariant is a property of a geometric configuration that is almost invariant under a class of imaging transformations. Formally, a geometric configuration is a QI if the linear term(s) in the Taylor series expansion of the configuration with respect to the parameters of the imaging transformation vanish. This has the effect of making the QI measure nearly constant over a large region of the viewing hemisphere, and rapidly diverging only as the angle between the view direction and the surface normal approaches large values. This behavior lends itself to probabilistic modeling and the use of reasoning schemes such as Bayesian evidence accrual. A detailed study of the variation of “invariant” features with viewpoint has been undertaken [13].

Intensity-based Invariants (II's) are functions of image intensities that yield values which are invariant to scene illumination and viewpoint. To date, some investigation of II's has been conducted for visible imagery, but practically none has been reported for non-visible imagery. Examples of II's in computer vision include color features for object recognition [14], [15], [16] and polarization cues for material identification [17]. A more direct example of this approach computes ratios of albedos of homogeneous image intensity patches within objects in visible imagery [18].

Non-visible modalities of sensing have been shown to greatly increase the amount of information that can be used for object recognition. A very popular and increasingly affordable sensor modality is thermal imaging - where non-visible radiation is sensed in the long-wave infrared (LWIR) spectrum of $8\mu m$ to $14\mu m$. The current generation of LWIR sensors produce images of contrast and resolution that compare favorably with broadcast television quality visible light imagery. However, the images are no longer functions of only surface reflectance. As the wavelength of the sensor transducer passband increases, emissive effects begin to emerge as the dominant mode of electromagnetic energy exitance from object surfaces. The radiation leaving a surface includes the reflected portion of the irradiation, as well as direct emissions. The term radiosity accounts for all of the energy leaving the surface [19]. The (primarily) emitted radiosity of LWIR energy has a strong dependence on internal composition, properties, and state of the object such as specific heat, density, volume, heat generation rate of internal sources, etc. This dependence may be exploited by specifying image-derived invariants that vary only if these parameters of the physical properties vary.

The derivation of thermophysical invariants (TI's) from non-visible wavelength imagery, the evaluation of the performance of these invariants, and their use in object recognition systems poses several advantages. The main advantage of this approach is the potential availability of a number of new (functionally independent) invariants that depend on internal compositional properties of the imaged objects. Note that it is possible to evaluate the behavior of thermophysical invariants using ground truth data consisting of images of objects of known composition and internal state. This additional information can be used to augment/complement the behavior of GI's. One way in which GI's can be integrated with TI's for object recognition is as follows: (1) Parametric curves and/or lines are extracted from an LWIR image. (2) The curves are used to compute GI's which are in turn used to hypothesize object identity and pose, and (3) TI's are computed for this hypothesis and compared to a stored model library for verification. Some details of this approach are presented later.

In this paper we first review a recently reported scheme that establishes thermophysical quasi-invariants from LWIR imagery. This scheme uses the principle of conservation of

energy at the surface of the imaged object to specify a functional relationship between the object's thermophysical properties (e.g., thermal conductivity, thermal capacitance, emissivity, etc.), scene parameters (e.g., wind temperature, wind speed, solar insolation), and the sensed LWIR image gray level. This functional form provides features that remain relatively constant despite changes in scene parameters/driving conditions. In this formulation the internal thermophysical properties play a role that is analogous to the role of parameters of the conics, lines and/or points that are used for specifying geometric invariants when analyzing visible wavelength imagery. Thus, in addition to the currently available techniques of formulating features that depend only on external shape and surface reflectance discontinuities, the phenomenology of LWIR image generation is used to establish new features that “uncover” the composition and thermal state of the object, and which do not depend on surface reflectance characteristics. However, this previous technique requires a great deal of scene information to derive the thermophysical features, and also requires radiometrically calibrated imagery.

Next, we extend an existing scheme for forming thermophysical invariant features by using principles of algebraic invariance theory [20]. The previous TAI approach depended on the use of radiometrically calibrated imagery, i.e. imagery where the relationship between the sensed gray scale values and the actual temperature of the imaged object is assumed known [21]. Since radiometrically calibrated LWIR imagery is not always available and in many cases such calibration is not possible, the previously reported interpretation algorithms are limited to a relatively small range of applications. The new approach presented in this paper allows the use of uncalibrated imagery, thus broadening the application of the overall approach. Furthermore, unlike the previous approach the new approach does not require any knowledge of the ambient conditions of the scene. It accounts for, and is tolerant to, variation in atmospheric attenuation from scene to scene, and also missing/unavailable measurement of the ambient temperature at the scene. This further detaches the object recognition process from the environmental conditions under which the object is imaged, and by requiring less *a priori* knowledge of the scene, the dependence of the feature on the intrinsic properties of the object is increased. The new TI approach is used to generate features in a model-based object recognition scheme. The results are

promising in that the features derived show strong intra-class stability - the feature value is constant for a given object class and under varying conditions. The features also exhibit good separability characteristics in inter-class tests - the feature values extracted from other object classes are well separated.

Finally, we show that the distribution of the TAI features can be accurately modeled by symmetric alpha-stable models. In previous work, we assumed that the TAI features would have a Gaussian distribution. Actually, the TAI is formed from the ratio of two approximately Gaussian distributed quantities, and hence tends to be close to a Cauchy distribution. We argue that a Gaussian classifier produces poor results, and a more appropriate classifier based on symmetric alpha-stable models is warranted. This approach is shown to yield robust classifier performance on very large data sets.

Another computer vision/image understanding task that is closely related to object recognition is the task of automatic site change detection. In one example of such a task, images are obtained, periodically, by an aircraft or satellite flying over a site to be monitored. The imagery is compared with known prior information or detailed site models to determine if any changes have occurred. For example, it may be important to detect if a patch of gravel or dirt has been replaced with a concrete or asphalt surface at some factory or construction site being monitored. Since some information is usually available of the site being monitored (in the form of site models), and also of the imaging parameters of the sensors, the site change detection task follows the paradigms of context-based vision and model-based vision. It is also closely related to the task of object recognition where a hypothesis of an object composed of different material types is verified or refuted. A particular site may be considered to be a composition of a specific collection of materials. A feature may be used to verify the existence of this composition. A change in the site should result in a feature value other than that expected for the original site. We discuss the application of our approach to site change detection and present results of analyzing real LWIR imagery.

The ideas presented in this paper are continuations and extensions of previous and ongoing research in thermophysical model-based interpretation of LWIR imagery. Section 2 describes relevant past work on thermophysical approaches for interpreting infrared im-

agery. A description of using principles of algebraic invariance to formulate thermophysical invariants is presented in section 3, followed by extensions to deal with radiometrically uncalibrated IR imagery. Symmetric Alpha-Stable distributions are explained in section 4. Preliminary experimental results of applying this new approach to real imagery are presented in section 5, which is followed by a discussion of the behavior of the new method, issues to be considered in using this method for object recognition, and issues that remain to be explored.

II. PAST THERMOPHYSICAL APPROACHES TO IR IMAGE ANALYSIS

A. *Heuristic Methods*

An intuitive approach to thermophysical interpretation of LWIR imagery is given in [22]. This approach rests upon the following observation, termed the “Thermal History Consistency Constraint” and analogous to Lowe’s well known Viewpoint Consistency Constraint [23]: “The temperature of all object features for a passive object must be consistent with the heat flux transfer resulting from exposure to the same thermal history.” In [22] this constraint is exploited by analyzing objects to locate components that are similar in terms of thermophysical properties and then examining a temporal sequence of calibrated LWIR data to experimentally assess the degree to which such thermophysically similar components exhibit similar temperature state temporal behavior. Such analysis was shown to lead to formulation of simple intensity ratio features. No experimentation was done with multiple objects to examine between and within-class separation, so little can be drawn in the way of a substantive conclusion with respect to utility as an object identification technique.

B. *A Physics-Based Model*

A physics-based approach has been attempted to establish invariant and quasi-invariant features which depend only on thermophysical object properties. Such an approach requires that a model be developed based on the principle of the conservation of energy at an elemental surface patch on the object. An overview of this approach is presented below. The use of this model in a previously reported technique is then presented and a new approach using algebraic invariance theory on this model is described in section 3.

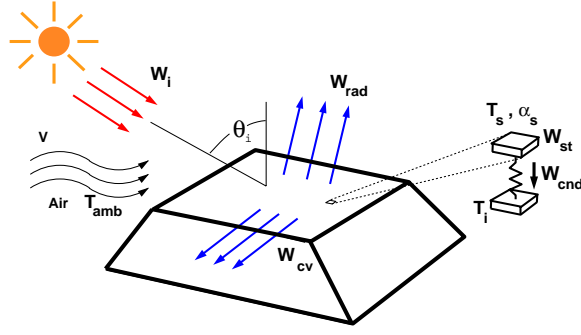


Fig. 1. Energy exchange at the surface of the imaged object. Incident energy is primarily in the visible spectrum. Surfaces lose energy by convection to air, via radiation to the atmosphere, and via conduction to the interior of the object. An elemental volume at the surface is shown. Some of the absorbed energy is stored in the elemental volume, while another portion is conducted into the interior of the object.

Consider an infinitesimal volume at the surface of the imaged object (figure 1). The surface exchanges energy with the environment via different mechanisms as discussed below. In the following, for the sake of convenience, we use the term ‘energy’ in short for energy measured per unit time. The energy absorbed by the surface equals the energy lost to the environment.

$$W_{abs} = W_{lost} \quad (1)$$

Energy absorbed by the surface (per unit surface area) is given by

$$W_{abs} = W_I \cos\theta_I \alpha_s, \quad (2)$$

where, W_I is the incident solar irradiation on a horizontal surface per unit area and is given by available empirical models (based on time, date and latitude of the scene) or by measurement with a pyranometer, θ_i is the angle between the direction of irradiation and the surface normal, and α_s is the surface absorptivity which, for opaque objects, is related to the visual reflectance ρ_s by $\alpha_s = 1 - \rho_s$. Note that it is reasonable to use the visual reflectance to estimate the energy absorbed by the surface since approximately 90% of the energy in solar irradiation lies in the visible wavelengths [19].

The energy lost by the surface to the environment was given by

$$W_{lost} = W_{cv} + W_{rad} + W_{cnd} + W_{st}, \quad (3)$$

where, W_{cv} denotes the energy (per unit surface area) convected from the surface to the air which has temperature T_{amb} and velocity V , W_{rad} is the energy (per unit surface

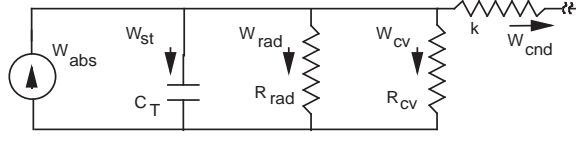


Fig. 2. The equivalent thermal circuit for the extended model that separates the stored energy component and the conduction component to the interior of the object.

area) lost by the surface to the environment via radiation and W_{cnd} denotes the energy (per unit surface area) conducted from the surface into the interior of the object. The radiation energy loss is computed from:

$$W_{rad} = \epsilon \sigma (T_s^4 - T_{amb}^4), \quad (4)$$

where, σ denotes the Stefan-Boltzmann constant, T_s is the surface temperature of the imaged object, and T_{amb} is the ambient temperature. Assume ϵ for the atmosphere is equal to ϵ for the imaged object. This assumption is reasonable if the objects are not uncoated metals. This assumption may not hold if the imaged surface is exposed or unoxidized metal which is usually rare.

The convected energy transfer is given by

$$W_{cv} = h(T_s - T_{amb}) \quad (5)$$

where, h is the average convected heat transfer coefficient for the imaged surface, which depends on the wind speed, thermophysical properties of the air, and surface geometry [19].

The equivalent thermal circuit for the surface is shown in figure 2. Lateral conduction from the elemental volume at the surface is assumed negligible since the temperature of the material adjacent to the surface volume under consideration may be assumed to be similar. In general, the internal temperature of the material will be different from that at the surface. The energy flow due to this gradient is expressed as the conducted energy, $W_{cnd} = -k dT/dx$, where k is the thermal conductivity of the material, and x is distance below the surface. Since we are considering an elemental volume at the surface this can be written in finite difference form: $W_{cnd} = -k \frac{(T_s - T_{int})}{\Delta x}$, for infinitesimal Δx . W_{cnd} is also expressed in units of energy flowing across unit area.

Within the elemental volume, the temperature is assumed uniform, and the increase in the stored energy given by $W_{st} = C_T \frac{dT_s}{dt}$, where C_T is the thermal capacitance for the

material of the elemental surface volume. This is given by $C_T = DVc$, where D is the density of the surface material, V is the elemental volume, and c is the specific heat. Again, W_{st} is expressed in units of energy per unit surface area. The equivalent circuit (shown in figure 2) have resistances given by:

$$R_{cv} = \frac{1}{h} \quad R_{rad} = \frac{1}{\epsilon\sigma(T_s^2 + T_{amb}^2)(T_s + T_{amb})} \quad \text{and} \quad R_{cnd} = \frac{1}{k}. \quad (6)$$

C. Establishing a Quasi-Invariant

The physics-based model described above was used to interpret registered IR and visual imagery from an outdoor scene [24]. First, a low Biot number was assumed, viz., the surface was considered to be a thin plate, hence $W_{cnd} = 0$. A simplified shape-from-shading approach was used to compute $\cos\theta_I$ and α_s from the visual image. The surface temperature, T_s , was estimated from the thermal image based on an appropriate model of radiation energy exchange between the surface and the infrared camera. W_I is given by available empirical models (as previously mentioned). The wind speed, and ambient temperature are also measured for the scene. Thus the energy flows, W_{abs} , W_{cv} , W_{rad} and hence W_{st} may be computed from the image and scene information.

It is clear from figure 2 that the conduction energy term W_{st} depends on the lumped thermal capacitance C_T of the object and can be used to describe the object's ability to sink/source thermal radiation, a feature shown to be useful in discriminating between different classes of objects. In order to minimize the feature's dependence on differences in absorbed energy flux, a normalized feature was defined to be the ratio $R = W_{st}/W_{abs}$. The values were found to be lowest for vehicles, highest for vegetation and in between for buildings and pavements. Classification of objects using this property value is discussed in [25].

Although this approach for integrated analysis of thermal and visual imagery is powerful in that it makes available features that are completely defined by internal object properties, the thermophysical feature estimates were not sufficiently reliable due to errors in segmentation and registration of the thermal and visual image pairs, and the noise-sensitivity of shape-from-shading techniques used in computing relative orientation of the surface [26]. A statistically robust scheme for computing the thermophysical feature R was proposed to minimize this drawback [27]. However, the computational complexity for

such a technique is very high. Another limitation in the previous formulation is that a low Biot number was assumed, viz., the surface was assumed to be a thin plate, which is rarely satisfied in practise. Also, the technique requires *a priori* knowledge of several surface and scene parameters such as emissivity, wind speed, solar insolation, etc, which in many applications are unavailable. Even in those situations where such information is available, the thermophysical feature, R , is only weakly invariant. While separation between classes is preserved, the range of values of R for each class is observed to vary with time of day and season of year. Also, the feature R is able to only separate very broad categories of objects, such as automobiles, buildings, and vegetation - it lacks the specificity to differentiate between different models of vehicles.

An improved formulation that attempts to overcome these limitations is described in section 3, wherein the feature is constrained to be invariant to affine transformations of the driving (scene) conditions.

III. THERMOPHYSICAL ALGEBRAIC INVARIANTS (TAI's)

An improved approach for computing invariant features that depend on the internal, thermophysical properties of the imaged object, and that are invariant to driving (scene and surface) parameters is based on a reformulation of the model outlined in section 2. In this formulation we explicitly eliminate the requirement that the ambient temperature be known, and we eliminate the requirement that radiometric calibration be known. First, to account for reasonable values of Biot numbers, viz. for objects other than thin plates, W_{cnd} is no longer assumed to be zero. Next, the radiosity at the surface of an object can be approximated to be linearly dependent on surface temperature. Consider equation (4) for the radiation energy loss term. A standard simplification of this expression results in the following form [19],

$$W_{rad} = \epsilon \sigma (T_s + T_{amb})(T_s^2 - T_{amb}^2)(T_s - T_{amb}) = h'(T_s - T_{amb}), \quad (7)$$

where h' is assumed to be constant over a specific range of temperatures. Note that when the variation in scene temperature is no more than $\pm 50^\circ C$ the error due to the linearity assumption is less than 10% (figure 3), which we have found to be comparable to the accuracy possible by radiometric calibration.

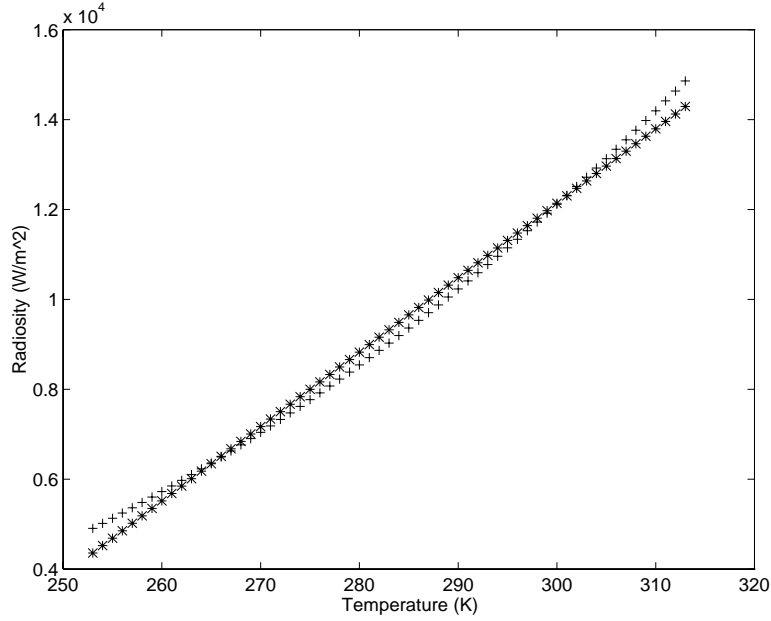


Fig. 3. Approximating radiosity to be a linear function of temperature. The error due to this approximation is less than 10% for $T \in [T_o - 50^\circ\text{C}, T_o + 50^\circ\text{C}]$. However, in our field tests the range of temperatures was smaller, $T \in [T_o - 20^\circ\text{C}, T_o + 40^\circ\text{C}]$, and the error in the approximation was found to be less than 4%.

This observation also implies that the gray level, L_s , of the LWIR image is related to the surface temperature, T_s , of the object's surface by a linear relationship,

$$L_s = \frac{1}{\beta}(T_s + \mu). \quad (8)$$

Using the above approximations the energy balance equation, $W_{abs} = W_{rad} + W_{cv} + W_{st} + W_{cnd}$ may be now rewritten in the following linear form:¹

$$a^1 x_1 + a^2 x_2 + a^3 x_3 + a^4 x_4 + a^5 x_5 = 0. \quad (9)$$

where

$$\begin{aligned} a^1 &= \cos\theta_I & x_1 &= W_I \alpha_s \\ a^2 &= L_s & x_2 &= -\beta(h + h') \\ a^3 &= C_T & x_3 &= -\frac{dT_s}{dt} \\ a^4 &= k & x_4 &= -T_s + T_{int} \\ a^5 &= 1 & x_5 &= -(T_{amb} + \mu)(h + h') \end{aligned} \quad (10)$$

¹Here, we use the Einstein notation to denote the image-based measurement vector as a contravariant tensor, a^i , while the changing scene conditions form a covariant tensor, x_i . Therefore, $a^i x_i = 0$.

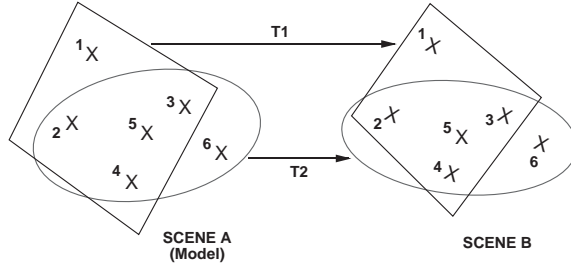


Fig. 4. We need a collection of five points in 5D measurement space to compute the affine transformation, T_i , between two scenes. Two different sets of 5 points each can be used to define an absolute invariant provided $\det(T_1) = \det(T_2)$.

Any pixel in the LWIR image of an object will yield a 5-D measurement tensor, \mathbf{a} . The LWIR pixel intensity provides a^2 . The values for a^1 , a^3 , and a^4 are provided by the hypothesized model identity and pose. The “driving conditions”, or unknown scene parameters that change from scene to scene are described by x_i . For each pixel in the thermal image eqn (10) defines a hyperplane in 5-D space. Note that the last element of the measurement tensor is always unity.

A. An Algebraic Invariance Formulation

Consider two different LWIR images of a scene obtained under different scene conditions and from different viewpoints. Consider N points on the object that (a) are visible in both views, and (b) have been selected to lie on different components of the object which differ in material composition and/or surface normal direction. Assume (for the nonce) that the object pose for each view, and point correspondence between the two views are available (or hypothesized). A point in each view yields a contravariant tensor a^i as defined by eqn (10). Let the collection of these tensors be denoted by $a_k^i, k = 1, 2, \dots, N$ for the first scene/image and $b_k^i, k = 1, 2, \dots, N$ for the second scene. For the k -th point we denote the measurement tensor as \mathbf{a}_k for the first view, and as \mathbf{b}_k for the second view, and the driving conditions tensor as \mathbf{x}^k .

We assume that the scene/driving conditions, \mathbf{x}^k for the first view and \mathbf{y}^k for the second view, are related by an affine transformation. The justification of this assumption is discussed below. We have found, empirically, that this assumption holds when the points are selected using the method discussed later in this paper. Since the \mathbf{x}^k are transformed

affinely, then it follows that the \mathbf{a}_k are also transformed affinely. Note that an affine transformation from one scene to another is trivial to obtain if we have only five points that generate five non-coplanar tensors in our 5-D measurement space. Consider one such subset of 5 of the N points, and denote them as h, j, l, m , and n .

The determinant

$$d(\mathbf{a}_h \mathbf{a}_j \mathbf{a}_l \mathbf{a}_m \mathbf{a}_n) = \begin{vmatrix} a_h^1 & a_h^2 & a_h^3 & a_h^4 & a_h^5 \\ a_j^1 & a_j^2 & a_j^3 & a_j^4 & a_j^5 \\ a_l^1 & a_l^2 & a_l^3 & a_l^4 & a_l^5 \\ a_m^1 & a_m^2 & a_m^3 & a_m^4 & a_m^5 \\ a_n^1 & a_n^2 & a_n^3 & a_n^4 & a_n^5 \end{vmatrix} = |A| \quad (11)$$

defines the “volume” of the oriented parallelepiped formed by the pencil of the five contravariant tensors $\mathbf{a}_h, \mathbf{a}_j, \mathbf{a}_l, \mathbf{a}_m, \mathbf{a}_n$. The above determinant is a relative invariant to the affine transformation [28], i.e.,

$$d(\mathbf{a}_h \mathbf{a}_j \mathbf{a}_l \mathbf{a}_m \mathbf{a}_n) = \delta_{hjlmn} \times d(\mathbf{b}_h \mathbf{b}_j \mathbf{b}_l \mathbf{b}_m \mathbf{b}_n) \quad (12)$$

where δ_{hjlmn} is the determinant of the affine transformation, T_{hjlmn} , which relates the measurement tensors, i.e., $\mathbf{a}_k = \mathbf{b}_k T_{hjlmn}$, $k \in \{h, j, l, m, n\}$.

Consider another set of five points in which at least one point is different from the previous set. Denote this second set as $\{p, q, r, s, t\}$. Again, assume that the measurement tensors for this collection of points undergo an affine transformation from the first scene to the second, and denote this transformation by T_{pqrst} .

$$d(\mathbf{a}_p \mathbf{a}_q \mathbf{a}_r \mathbf{a}_s \mathbf{a}_t) = \delta_{pqrst} \times d(\mathbf{b}_p \mathbf{b}_q \mathbf{b}_r \mathbf{b}_s \mathbf{b}_t) \quad (13)$$

where $\delta_{pqrst} = \det(T_{pqrst})$. Hence, if $\delta_{hjlmn} = \delta_{pqrst}$, then we can define an absolute invariant as

$$I = \frac{d(\mathbf{a}_h \mathbf{a}_j \mathbf{a}_l \mathbf{a}_m \mathbf{a}_n)}{d(\mathbf{a}_p \mathbf{a}_q \mathbf{a}_r \mathbf{a}_s \mathbf{a}_t)} = \frac{|A|}{|\hat{A}|} \quad (14)$$

where A and \hat{A} are measurement matrices formed by the tensors indicated above.

Note that the existence of affine transformations T_{hjlmn} and T_{pqrst} is easy to ensure by selecting the points that lie on different material types and/or have different surface normals. However, the existence and selection of two sets of five points such that $\delta_{hjlmn} = \delta_{pqrst}$ holds is crucial to the existence and determination of an absolute invariant. Our experimental investigation shows that point sets that satisfy this equivalence class of transformations are

plentiful on any real, complex object such as a vehicle. The thermophysical justification for the existence of this equivalence class is being addressed in our ongoing work.

The selection of the two sets (with five points in each) that satisfy this equivalence relationship may be attempted as a data-driven training task as follows. LWIR imagery from different object classes are obtained at different times of day and different seasons of the year. N points are picked on an object – on distinctive components that differ in material composition and/or surface normal. Consider the image from time t_u and the image from t_v , $u \neq v$. The measurements at t_u along with the hypothesis of the identity of the object form the tensors \mathbf{a}_k . Similarly, image information at time t_v is used to form the measurement tensors \mathbf{b}_k .

All combinations of two sets of five points each, $\{h, j, l, m, n\}$ and $\{p, q, r, s, t\}$, are examined. The measurement matrices $(\mathbf{a}_h \mathbf{a}_j \mathbf{a}_l \mathbf{a}_m \mathbf{a}_n)$, $(\mathbf{b}_h \mathbf{b}_j \mathbf{b}_l \mathbf{b}_m \mathbf{b}_n)$, $(\mathbf{a}_p \mathbf{a}_q \mathbf{a}_r \mathbf{a}_s \mathbf{a}_t)$, and $(\mathbf{b}_p \mathbf{b}_q \mathbf{b}_r \mathbf{b}_s \mathbf{b}_t)$ are constructed. The transformations T_{hjlmn} and T_{pqrst} , if they exist, and their determinants δ_{hjlmn} , and δ_{pqrst} are computed. The two sets that best satisfy $\delta_{hjlmn} = \delta_{pqrst}$ for different choices of pairs of scenes/images, i.e. different choices of t_u and t_v , are selected. With N points, the number of possible choices of the pair of sets of points is given by

$$n_N = \frac{1}{2} \left(\frac{N!}{(N-5)!5!} \right) \left(\frac{N!}{(N-5)!5!} - 1 \right) \quad (15)$$

In order for the invariant feature to be useful for object recognition the value of I must be different if the measurement vector is obtained from a scene that does not contained the hypothesized object and/or the hypothesized pose is incorrect. A search for the best sets of points that both identify the object and separate the classes must be conducted over the n_N point sets. The point sets may be rated for their intra-class invariance, then the best choices may be used to evaluate their inter-class separability.

B. Employing TAI's for Object Recognition / Site Change Detection

The feature computation scheme formulated above is suitable for use in an object recognition system that employs a hypothesize-and-verify strategy. The scheme would consist of the following steps:

1. extract geometric features, e.g., lines and conics.

2. for image region, r , hypothesize object class, k , and pose using, for example, geometric invariants as proposed by Forsyth, et al [1],
3. use the model of object k and project visible points labeled $i = 1, 2, \dots$ onto image region r using scaled orthographic projection,
4. for point labeled i in the image region, assign thermophysical properties of point labeled i in the model of object k ,
5. use the gray levels at each point and the assigned thermophysical properties, to compute the measurement matrices A and \hat{A} , and hence compute the feature $f^k(r) = |A|/|\hat{A}|$, and finally,
6. compare feature $f^k(r)$ with model prototype F_k to verify the hypothesis.

The application of this scheme for site change detection is straightforward. For a site being monitored, M different types of surfaces are selected *a priori* to produce a thermophysical affine invariant. Note that we must have $M > 5$. One may also be able to specify more than one TAI, and hence establish a feature vector. An LWIR image is first registered with the site using established techniques [29]. The gray levels from the M selected regions along with the known material properties are used to generate the TAI features. When one or more of the surfaces change (e.g., from gravel to concrete) then the feature (vector) computed from the scene under the hypothesis of the prior material types will produce a value different from that expected. The detection of the change is thus linked to the refutation of an incorrect hypothesis.

C. Reduced Dimension Forms

The linear form, eqn (9), must be slightly modified to facilitate feature specification in scenarios where the feature described above becomes undefined. Two such cases are (1) interpreting LWIR imagery acquired at night and (2) imaging an object on which all of the surface normals are parallel. For the nighttime case the solar insolation is nonexistent, W_{abs} as defined above is zero, and the energy balance model has only four terms. Hence, the measurement tensor is four dimensional. In this case we can simply consider sets of four points in evaluating the absolute invariant. The case where all of the visible object surfaces are oriented such that their normals are parallel is slightly more complex and requires consideration of the algebraic form.

Consider two sets of points from the same scene that are used to form the feature in eqn (14). As described above, the balance of energy equation must be satisfied at each of these points. The form of an equation for a point in the first set is

$$a_k^i x_i^k = 0, \quad i = 1 \dots 5, \quad k \in \{h, j, l, m, n\} \quad (16)$$

where the variable labeling is the same as that in eqn (10). Note that $a^5 = \cos \theta$ and $x_5 = W_I \alpha_s$. Similarly the form for a point in the second set is

$$\hat{a}_k^i \hat{x}_i^{k'} = 0, \quad i = 1 \dots 5, \quad k' \in \{p, q, r, s, t\} \quad (17)$$

where again the variable labeling is from eqn (10) and $\hat{a}^5 = \cos \theta$ and $\hat{x}_5 = W_I \hat{\alpha}_s$. Since the surface normals are parallel, $\cos \theta$ is the same for all points in the two sets that form the measurement matrices, A and \hat{A} . This will cause two of the columns of the measurement matrix of eqn (11) to be linearly dependent, and the feature value will be undefined in the original formulation eqn (14). Note also that the incident solar flux is also the same for all points in the two sets.

Now consider the eqns (16) and (17) expressed with the cosine terms separated out. The equation for the first set becomes,

$$a_k^i x_i^k + \cos \theta W_I \alpha_s^k = 0, \quad i = 1 \dots 4, \quad k \in \{h, j, l, m\}. \quad (18)$$

The second set is likewise defined,

$$\hat{a}_k^i \hat{x}_i^{k'} + \cos \theta W_I \hat{\alpha}_s^{k'} = 0, \quad i = 1 \dots 4, \quad k' \in \{p, q, r, s\} \quad (19)$$

Subtracting eqns (19) from (18) yields,

$$a_k^i x_i^k = \hat{a}_k^i \hat{x}_i^{k'} + \Phi_{(k,k')} \quad i = 1 \dots 4, \quad (k, k') \in \{(h, p), (j, q), (l, r), (m, s)\} \quad (20)$$

where $\Phi = \cos \theta W_I (\alpha_s^k - \hat{\alpha}_s^{k'})$, $(k, k') \in \{(h, p), (j, q), (l, r), (m, s)\}$.

Consider the construction of the measurement matrices \tilde{A} and $\hat{\tilde{A}}$ as described before in eqn (11), but which are now of size 4×4 and again are of full rank. The driving conditions tensors x_i and \hat{x}_i are used to construct the driving conditions matrices, \tilde{X} and $\hat{\tilde{X}}$ where each point specifies a column vector. The matrices, \tilde{A} , $\hat{\tilde{A}}$, \tilde{X} , and $\hat{\tilde{X}}$ span $\mathbb{R}^{4 \times 4}$. The driving condition matrices, \tilde{X} and $\hat{\tilde{X}}$ can be related by an affine transformation, and hence the measurement matrices \tilde{A} and $\hat{\tilde{A}}$ are related by an affine transformation. In order to express the transformation from one set of points to the other in a linear form, the measurement matrices and driving condition matrices are expressed in homogeneous

coordinates with the translation, Φ , augmenting the driving conditions matrix. Denote the homogeneous versions of the measurement and driving condition matrices as \tilde{A}_ψ , $\hat{\tilde{A}}_\psi$, \tilde{X}_ψ , and $\hat{\tilde{X}}_\psi$. The above relationships can be expressed in homogeneous coordinates as follows:

$$\begin{aligned}
 & \begin{pmatrix} a_h^1 & a_h^2 & a_h^3 & a_h^4 & 1 \\ a_j^1 & a_j^2 & a_j^3 & a_j^4 & 1 \\ a_l^1 & a_l^2 & a_l^3 & a_l^4 & 1 \\ a_m^1 & a_m^2 & a_m^3 & a_m^4 & 1 \\ 0 & 0 & 0 & 0 & 1 \end{pmatrix} \begin{pmatrix} x_1^h & x_1^j & x_1^l & x_1^m & 0 \\ x_2^h & x_2^j & x_2^l & x_2^m & 0 \\ x_3^h & x_3^j & x_3^l & x_3^m & 0 \\ x_4^h & x_4^j & x_4^l & x_4^m & 0 \\ 0 & 0 & 0 & 0 & 1 \end{pmatrix} \\
 &= \begin{pmatrix} \hat{a}_h^1 & \hat{a}_h^2 & \hat{a}_h^3 & \hat{a}_h^4 & 1 \\ \hat{a}_j^1 & \hat{a}_j^2 & \hat{a}_j^3 & \hat{a}_j^4 & 1 \\ \hat{a}_l^1 & \hat{a}_l^2 & \hat{a}_l^3 & \hat{a}_l^4 & 1 \\ \hat{a}_m^1 & \hat{a}_m^2 & \hat{a}_m^3 & \hat{a}_m^4 & 1 \\ 0 & 0 & 0 & 0 & 1 \end{pmatrix} \begin{pmatrix} \hat{x}_1^h & \hat{x}_1^j & \hat{x}_1^l & \hat{x}_1^m & 0 \\ \hat{x}_2^h & \hat{x}_2^j & \hat{x}_2^l & \hat{x}_2^m & 0 \\ \hat{x}_3^h & \hat{x}_3^j & \hat{x}_3^l & \hat{x}_3^m & 0 \\ \hat{x}_4^h & \hat{x}_4^j & \hat{x}_4^l & \hat{x}_4^m & 0 \\ \Phi_h & \Phi_j & \Phi_l & \Phi_m & 1 \end{pmatrix}. \tag{21}
 \end{aligned}$$

Representing the general linear transformation in homogeneous coordinates as $\tilde{X} = M\hat{\tilde{X}}$. Substituting the transformed variable

$$\tilde{A}_\psi \tilde{X}_\psi = \hat{\tilde{A}}_\psi M \hat{\tilde{X}}_\psi. \tag{22}$$

As in section 3.1 an absolute invariant is found when the following ratio remains constant from scene to scene

$$\frac{|\tilde{A}_\psi|}{|\hat{\tilde{A}}_\psi|} = |M|. \tag{23}$$

Since the augmentation of the \tilde{A} and $\hat{\tilde{A}}$ into homogeneous coordinates does not affect the value of the determinant then

$$\frac{|\tilde{A}|}{|\hat{\tilde{A}}|} = \frac{|\tilde{A}_\psi|}{|\hat{\tilde{A}}_\psi|} = |M|. \tag{24}$$

Thus we have shown that in the case where the visible surfaces of the imaged object have parallel normals an invariant feature can be derived by modeling the driving conditions transformation as a affine transformation. In either of the two cases of analyzing nighttime imagery or objects with parallel normals, a separate training phase is required for the specification of the invariant feature. In general, the choice of points for the reduced forms will be distinct from that of the full linear form.

IV. STATISTICAL MODELS FOR TAI FEATURE DISTRIBUTIONS

The TAI features are formed from the ratio of two determinants, each of which satisfies the central limit theorem conditions and is, therefore, asymptotically Gaussian. As a result, their ratio clearly deviates from Gaussianity and is, in fact, asymptotically Cauchy-distributed [30]. The performance of a Gaussian classifier applied on such a non-Gaussian feature is unacceptably low. Instead, a non-Gaussian classifier needs to be developed.

The signal processing and communication communities have recently reported work on real-time processing of a generalized class of “impulsive” distributions which contain the Gaussian and the Cauchy as special cases. This class, known as the *alpha-stable* class, is an appealing model for the distribution of TAI features. Since this class of distributions is relatively unfamiliar, we briefly summarize their key definitions and properties, concentrating on the subclass of *symmetric* alpha-stable distributions (S α S).

A univariate S α S probability density function (pdf) $f_\alpha(\gamma, \delta; \cdot)$ is best defined via the inverse Fourier transform integral [31]

$$f_\alpha(\gamma, \delta; x) = \frac{1}{2\pi} \int_{-\infty}^{\infty} \exp(i\delta\omega - \gamma|\omega|^\alpha) e^{-i\omega x} d\omega \quad (25)$$

and is completely characterized by the three parameters α (*characteristic exponent*, $0 < \alpha \leq 2$), γ (*dispersion*, $\gamma > 0$), and δ (*location parameter*, $-\infty < \delta < \infty$).

The characteristic exponent α relates directly to the heaviness of the tails of the S α S pdf. The smaller its value, the heavier the tails. The value $\alpha = 2$ corresponds to a Gaussian pdf, while the value $\alpha = 1$ corresponds to a Cauchy pdf. The dispersion γ is a measure of the spread of the pdf, similar to the variance of a Gaussian pdf. Finally, the location parameter, δ , is the point of symmetry of the pdf and equals its mean, whenever the mean is finite (i.e., for $1 < \alpha \leq 2$).

The non-Gaussian ($\alpha \neq 2$) S α S distributions maintain many similarities to the Gaussian distribution, but at the same time differ from it in some significant ways. For example, a non-Gaussian S α S pdf maintains the usual bell shape and, more importantly, non-Gaussian S α S random variables satisfy the linear stability property, i.e., they remain invariant to linear transformations. However, non-Gaussian S α S pdfs have much sharper peaks and much heavier tails than the Gaussian pdf. As a result, only their moments of order $p < \alpha$ are finite, in contrast with the Gaussian pdf which has finite moments of

arbitrary order. These and other similarities and differences between Gaussian and non-Gaussian S α S pdfs and their implications on the design of signal processing algorithms are presented in detail in the tutorial paper [32] or in the recent monograph [31] to which the interested reader is referred.

The three parameters of a S α S pdf may be estimated by several methods [32], [31], [33]. The location parameter, δ , may be estimated by the mean for $1 < \alpha \leq 2$ or the median for $0 < \alpha \leq 2$. However, the median is more efficient than the mean for all $\alpha < 2$ [33].

Once the location is known, then the exponent of the tails can be estimated using the $\log |S\alpha S|$ method [31].

$$\mathbf{Y} = \text{Var}(\log |\vec{X} - \hat{\delta}|) \quad (26)$$

$$\hat{\alpha} = \sqrt{\frac{2\pi^2}{12\mathbf{Y} - \pi^2}} \quad (27)$$

Finally, the dispersion γ can be determined from the data and the estimated δ and α .

$$\hat{\gamma} = \left(\frac{E(|\vec{X} - \hat{\delta}|^p)}{C(p, \hat{\alpha})} \right)^{\frac{\alpha}{p}} \quad (28)$$

$$C(p, \hat{\alpha}) = \frac{\Gamma(1 - \frac{p}{\alpha})}{\Gamma(1 - p) \cos(\frac{\pi}{2}p)}, \quad (29)$$

where p is the fractional lower order moment used to estimate the dispersion. Tsihrintzis and Nikias [33] show that a choice $0 < p < \alpha/2$ results in finite estimation error variance, while it has been experimentally observed that $p = \alpha/3$ is generally a good choice.

The maximum likelihood Cauchy classifier was proposed in [34] as a robust, yet simple test based on S α S processes. Figure 5 shows that the Cauchy classifier has a minimum probability of error for $\alpha = 1$ and is only slightly sub-optimal for any other α , including $\alpha = 2$, i.e. Gaussian distributions! The Gaussian classifier, on the other hand, degrades rapidly for $\alpha < 2$. The Cauchy classifier for a single feature value is:

$$t = \frac{\frac{\gamma_1}{\gamma_1^2 + (\mathbf{X} - \delta_1)^2}}{\frac{\gamma_2}{\gamma_2^2 + (\mathbf{X} - \delta_2)^2}} \underset{H_1}{\overset{H_0}{\geq}} \eta \quad (30)$$

where η can be varied to change the probability of detection and the probability of false alarm. If several independent samples are available, then the new test statistic is a sum of the log of the individual statistics. This new statistic can be shown to approach a Gaussian distribution and the probability of error can be asymptotically reduced on the

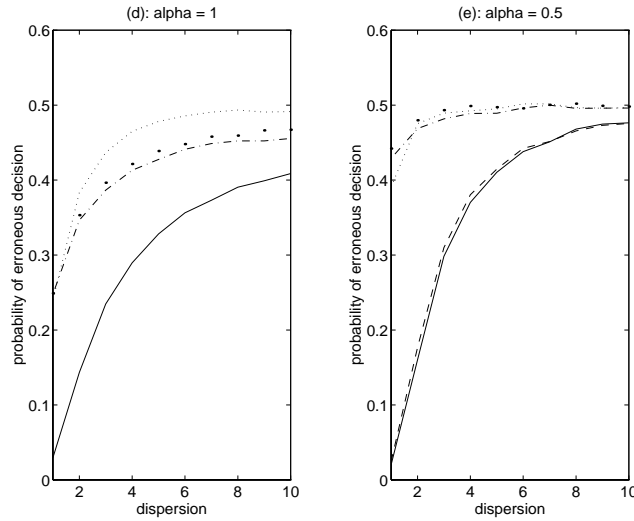


Fig. 5. Probability of Error for different classifiers. Solid line: optimal, Point line: linear (Gaussian), Dashed line: Cauchy. The dashed line and the solid line coincide in the plot on the left. The Cauchy classifier performs much better than the Gaussian classifier and only slightly worse than the optimal classifier. The dotted line and dash-dot line are for limiter-integrator schemes with different thresholds.

order of $1/n$, where n is the number of samples available. On the other hand, having multiple samples available to the original Gaussian classifier will not improve its results.

V. EXPERIMENTAL RESULTS

A. Object Recognition using TAIs

The method of computing thermophysical affine invariants discussed above was applied to real LWIR imagery acquired at different times of the day. Four types of vehicles were imaged: a van, a truck, a tank, and a car (figures 6). Several points were selected (as indicated in the figures) on the surfaces of different materials and/or orientation. The measurement tensor given by eqn (10) was computed for each point, for each image/scene.

The method used to select optimal sets of points $\{i, j, l, m, n\}$ and $\{p, q, r, s, t\}$ was similar to that described in section 3 – however, instead of using the equivalence of the determinants of the two affine transformations as the selection criterion, we used the variance in the values of the feature computed for different scenes containing the object, i.e., images obtained at different times of the day. Many different pairs of five-point-sets yielded features with low variance from scene to scene.

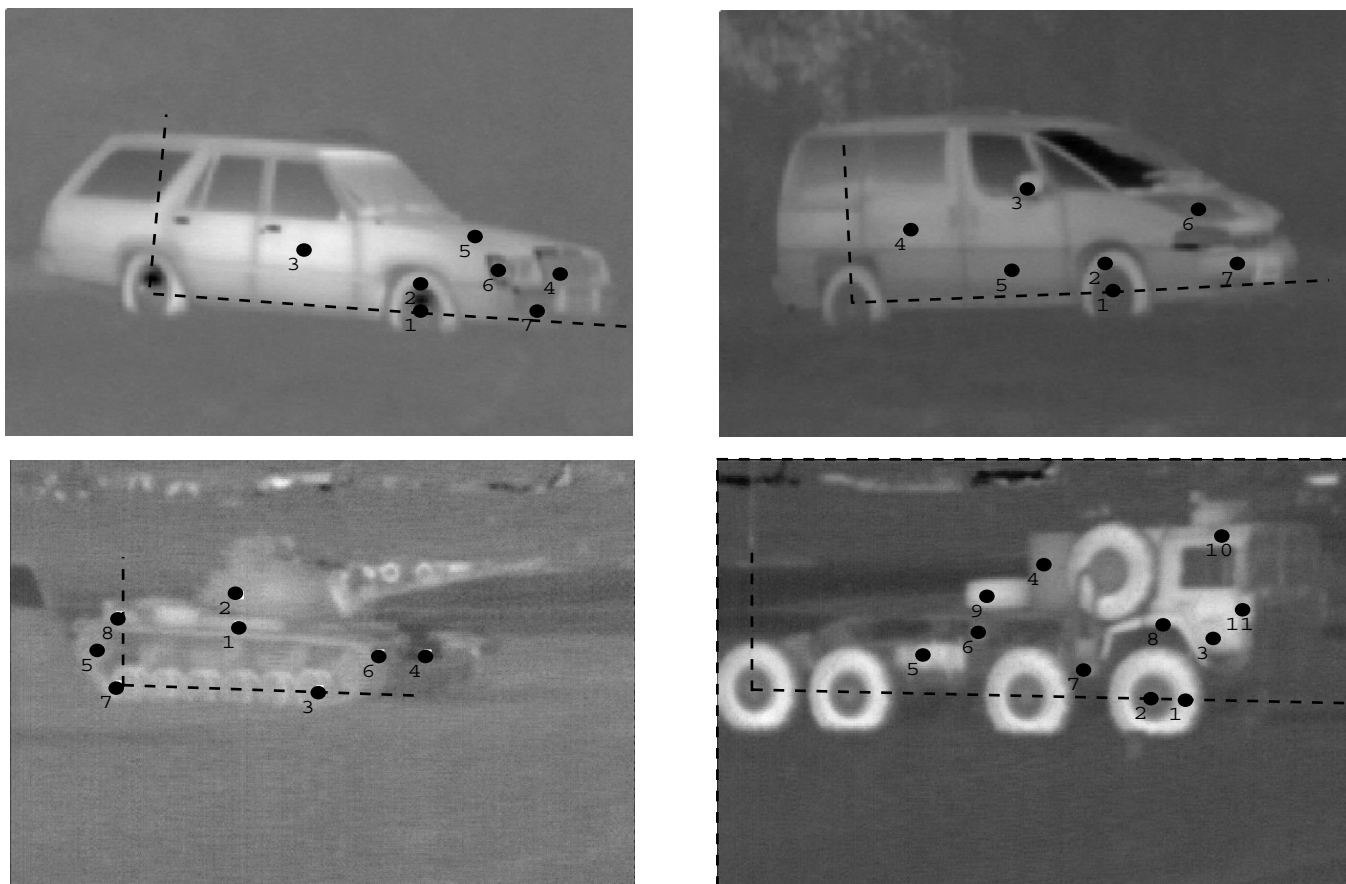


Fig. 6. The vehicles used to test the object recognition approach, (from top left clockwise) car, van, truck, and tank. The axis superimposed on the image show the object centered reference frames. The numbered points indicate the object surfaces used to form the measurement matrices. These points are selected such that there are a variety of different materials and/or surface normals within the set.

As mentioned in section 3, one must consider inter-class behavior as well as intra-class behavior. To investigate this we adopted the following procedure. Given an image of a vehicle, (1) assume the pose of the vehicle is known, then (2) use the front and rear wheels to establish an object centered reference frame. The center of the rear wheel is used as the origin, and center of the front wheel is used to specify the direction and scaling of the axes. The coordinates of the selected points are expressed in terms of this 2D object centered frame. For example, when a van vehicle is hypothesized for an image actually obtained of a car or some unknown vehicle, the material properties of the van are used, but image measurements are obtained from the image of the car at locations given by transforming

Time of Day	Hypothesis: Van Data from: Van	Hypothesis: Van Data from: Car	Hypothesis: Van Data from: Truck	Hypothesis: Van Data from: Tank
9 am	13.7716	8.6475	4.4318	10.5850
10 am	13.2269	10.7857	3.7986	15.0399
11 am	13.0597	11.0486	5.2089	11.2887
12 n	12.8853	10.1151	2.8861	22.1023

TABLE I

INTER-CLASS VARIATION VS. INTRA-CLASS VARIATION FOR FEATURE A-1, CONSISTING OF POINT SETS $\{2, 3, 4, 6, 7\}$, and $\{1, 4, 5, 6, 7\}$. THERMOPHYSICAL PROPERTIES ARE CHOSEN FOR THE VAN HYPOTHESIS. THE FIRST COLUMN SHOWS FEATURE VALUES COMPUTED WHEN THE CORRECT HYPOTHESIS IS MADE AND THE MEASUREMENT TENSOR IS OBTAINED FROM THE VAN. THE REMAINING COLUMNS SHOW THE RESULTS WHEN AN INCORRECT HYPOTHESIS IS MADE, I.E. DATA ARE COLLECTED FROM THE RESPECTIVE OBJECTS.

the coordinates of the van points (in the van center coordinate frame) to the image frame computed for the unknown vehicle. Table I shows inter-class and intra-class variation when a van is hypothesized, and for images obtained at four different times in the day. Table II shows inter-class and intra-class variation when the car is hypothesized.

B. Site Change Detection Using Ground Truth Data

The usefulness of these thermophysical invariant features for site change detection tasks was examined, experimentally, by analyzing “ground truth” data gathered from a scene as well as a temporal sequence of LWIR imagery from a scene. The first data set consisted of temperature measurements acquired from thermocouples implanted in various types of materials placed in an outdoor scene. The data were collected over a period of five days in mid-November. The collection includes varying weather conditions and has extensive records of the atmospheric pressure, ambient temperature, lighting conditions, etc. The measurements were recorded at closely spaced intervals of a few minutes. The materials included sod, clay, gravel, concrete, asphalt, and aluminum. Extensive modeling of the test site has been done, and simulations have reproduced the actual data to within $0.5^{\circ}C$.

Time of Day	Hypothesis: Car Data from: Car	Hypothesis: Car Data from: Van	Hypothesis: Car Data from: Truck	Hypothesis: Car Data from: Tank
9 am	0.4794	28.4142	2.0739	-3.9863
10 am	0.5464	-4.2408	4.8332	-1.7688
11 am	0.4286	0.9313	1.0922	-0.8577
12 n	0.4017	3.8774	0.6181	-0.7631

TABLE II

INTER-CLASS VARIATION VS. INTRA-CLASS VARIATION FOR FEATURE A-2, CONSISTING OF POINT SETS $\{1, 2, 4, 6, 7\}$, and $\{1, 2, 4, 5, 7\}$. THERMOPHYSICAL PROPERTIES ARE CHOSEN FOR THE CAR HYPOTHESIS. THE FIRST COLUMN SHOWS FEATURE VALUES COMPUTED WHEN THE CORRECT HYPOTHESIS IS MADE AND THE MEASUREMENT TENSOR IS OBTAINED FROM THE CAR. THE REMAINING COLUMNS SHOW THE RESULTS WHEN AN INCORRECT HYPOTHESIS IS MADE, I.E. DATA ARE COLLECTED FROM THE RESPECTIVE OBJECTS.

Consider a feature constructed (as described in section 3) using point sets {Grass, Clay, Gravel, Asphalt, Aluminum} and {Grass, Clay, Concrete, Asphalt, Aluminum}. The distribution of the value of this feature was computed when the measurements were obtained from the correctly hypothesized materials. The average value of the feature was -91.4, and the standard deviation was 1.7. Next, measurements for one of the hypothesized materials was obtained from a different material – to mimic the situation where one of the materials in the site is changed to a different one. The mean and standard deviation were computed for the feature value under this erroneous hypothesis. For change detection we should notice a significant difference in feature values computed under correct and wrong hypotheses. The feature’s behavior under different wrong hypotheses is summarized in table III.

Unfortunately, as we increased the number of data points considered, the variance of the thermophysical invariant increased rapidly. We also noted that the variance did not appear to converge. This is a clear indication that the thermophysical invariants do not fit a Gaussian model. Hence, that S α S model and a classifier based on this model were adopted. This scheme was tested on large data sets as discussed below.

Data from	Hypothesized Material					
	Grass	Clay	Gravel	Concrete	Asphalt	Aluminum
Grass	-91.4, 1.7	-91.2, 1.6	-91.1, 2.0	-91.5, 2.3	-90.0, 6.2	-92.0, 5.3
Clay	-72.8, 40.2	-91.4, 1.7	-72.9, 40.2	-91.7, 3.4	-74.4, 42.7	-80.0, 6.1
Gravel	-73.6, 40.8	-70.1, 39.3	-91.4, 1.7	-91.1, 0.1	16.4, 38.8	-84.0, 5.1
Concrete	-89.9, 0.8	-89.7, 0.4	-91.0, 0.1	-91.4, 1.7	-110.4, 0.1	-98.5, 6.2
Asphalt	-56.4, 31.8	-108.9, 90.3	17.8, 50.1	-110.1, 3.9	-91.4, 1.7	-87.9, 7.5
Aluminum	-90.9, 1.7	-91.0, 1.6	-91.2, 1.6	-91.1, 1.6	-91.6, 1.5	-91.4, 1.7

TABLE III

THE (MEAN, STANDARD DEVIATION) VALUES FOR A FEATURE CONSTRUCTED USING POINT SETS {GRASS, CLAY, GRAVEL, ASPHALT, ALUMINUM} AND {GRASS, CLAY, CONCRETE, ASPHALT, ALUMINUM}. THE VALUES OF THIS FEATURE WERE COMPUTED WHEN THE MEASUREMENTS WERE OBTAINED FROM THE CORRECTLY HYPOTHESIZED MATERIALS AND ALSO FOR SPECIFIC ERRONEOUS HYPOTHESES. DATA CONSISTED OF TEMPERATURE MEASUREMENTS FROM THERMOCOUPLES.

C. Site Change Detection Using Real Uncalibrated IR Imagery

In order to test the above ideas on a large collection of real imagery, we first acquired a temporal sequence of IR imagery from an outdoor scene containing asphalt, concrete, dirt, fiberglass, iron, rock, and wood (figure 7). The scene was imaged at 7 different times over a 2 day period. The correct material hypothesis constitutes one class, and an incorrect hypothesis results from the change of one specific material type to another. The reduced dimensional TAI discussed in section 3.3 was used to specify features. A TAI feature was found that could best detect each change of material. For each (correct or incorrect) hypothesis, the image data produced 10^9 unique values of the TAI feature! The Gaussian model produced estimates of the variances on the order of 10^5 – a clear indication of infinite variance [31]. The symmetric alpha-stable models, on the other hand, are an excellent fit, and classifiers were constructed based on these models to separate the correct and erroneous hypotheses.

We discuss, for the purposes of illustration, one specific thermophysical invariant that was chosen to detect a material change from slate to concrete. Figure 8(a) illustrates that



Fig. 7. (a) A visual image of the scene used for these experiments. Materials include Asphalt, Concrete, Dirt, Fiberglass, Iron, Slate, and Wood. (b) A corresponding long-wave infrared (LWIR) image. The scene was imaged at 7 different times over a 2 day period.

the amplitude probability distribution of the feature and the alpha-stable model agree very well. Figure 8(b) shows that the feature distribution under an incorrect hypothesis can also be modeled by a SoS distribution. This clearly indicates that classifiers based on SoS processes will perform better than conventional classifiers designed under the Gaussian assumption.

Using the Cauchy classifier on the data that were modeled in Figure 8, one can achieve a $\text{Pr}[\text{error}] = 2\%$. The Gaussian classifier, on the other hand, results in $\text{Pr}[\text{error}] = 49.9\%$! Therefore the Gaussian classifier will not be able to detect if concrete had been poured over slate, but the Cauchy classifier can do so with a low probability of missed change detection.

Table IV shows a complete set of models for the TAI constructed using point sets {Wood, Slate, Dirt, Fiberglass} and {Slate, Dirt, Concrete, Fiberglass}. The distribution of the value of this feature was computed when the measurements were obtained from the correctly hypothesized materials. The median value of the feature was 0.5, the characteristic

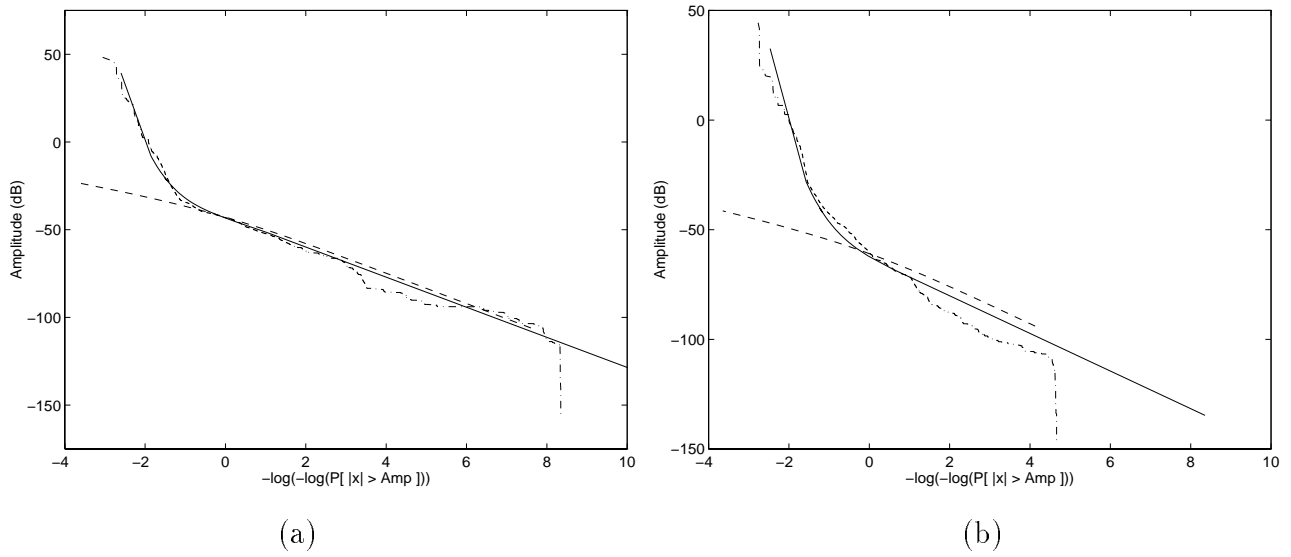


Fig. 8. (a) Theoretical S&S Amplitude Probability Distribution (APD) with $\alpha = 1.3$ and $\gamma = 0.001$ ($\delta = 0.1325$) matches the correct hypothesis data very well. The dashed line is the best Gaussian (hand-fitted $\sigma = .008$) approximation. Notice that in the tail region (the upper-left curved part) the Gaussian model diverges from the data. (b) An incorrect hypothesis can also be modeled very well ($\alpha = 0.8$, $\gamma = 0.0075$, and $\delta = 0.0095$, Gaussian $\sigma = .001$).

exponent was 1.2, and the dispersion was 1.1. Next, measurements for one of the hypothesized materials was obtained from a different material – to mimic the situation where one of the materials in the site is changed to a different one. The model parameters were computed for each of these features. For change detection we should notice a significant difference in feature values computed under correct and incorrect hypotheses. We observe such behavior for specific material changes, e.g. slate to concrete (0.91, 1.8, -3), and wood to iron (0.99, 0.41, 1). Notice that the variations due to incorrect hypothesis are neither symmetric, nor always separable. Also, notice when we hypothesize wood and the material is actually concrete, or when we hypothesize concrete and the material is actually wood, the dispersion becomes very large! This occurs because the point set in question differs only in these two materials. If one erroneously hypothesizes these materials as we’ve done, then the rank of the matrices will become singular, and the ratio will become very erratic. This strongly suggests a very simple method of detecting incorrect hypothesis given multiple data samples and different sets of TAIs (i.e. a rank test, or large dispersion).

We can combine the results of several different “good” TAIs to achieve the smallest

$(\hat{\alpha}, \hat{\gamma}, \hat{\delta})$	Hypothesized Material				
Actual	Wood	Slate	Dirt	Concrete	Fiberglass
Wood	1.2, 1.1, 0.5	0.78, 1.2, -0.5	1.1, 0.23, 0.4	1.7, 10^{11} , 0.8	1.3, 0.05, 0.02
Slate	1.5, 550, -0.2	1.2, 1.1, 0.5	1.1, 5.7, 0.6	0.81, 320, 2	1.1, 0.37, 0.6
Dirt	1.4, 410, 0.3	1.3, 8.3, 1	1.2, 1.1, 0.5	0.85, 0.76, 0.8	1, 0.24, 0.2
Iron	0.99, 0.41, 1	1.8, 0.05, -0.6	1, 0.21, 0.3	1.6, 0.06, 0.4	1.5, 0.03, -0.4
Concrete	1.5, 10^4 , 0.7	0.91, 1.8, -3	1.2, 0.29, 0.4	1.2, 1.1, 0.5	1.2, 0.16, -0.1
Asphalt	1.3, 42, 0.5	0.94, 1.1, 1	1.2, 0.25, 0.4	0.76, 0.54, 0.5	1.2, 0.32, 0.04
Fiberglass	1.5, 400, -0.07	1.1, 0.29, 0.6	1.1, 0.27, 0.5	0.71, 34, 0.9	1.2, 1.1, 0.5

TABLE IV

THE $(\hat{\alpha}, \hat{\gamma}, \hat{\delta})$ VALUES FOR A FEATURE CONSTRUCTED USING POINT SETS {WOOD, SLATE, DIRT, FIBERGLASS} AND {SLATE, DIRT, CONCRETE, FIBERGLASS}. THE VALUES OF THIS FEATURE WERE COMPUTED WHEN THE MEASUREMENTS WERE OBTAINED FROM THE CORRECTLY HYPOTHESED MATERIALS AND ALSO FOR SPECIFIC ERRONEOUS HYPOTHESES.

probability of error. The combined probabilities of error after testing approximately 1/3 of the possible TAI's are summarized in Table V. Five different TAIs were combined to achieve the results shown in this table. Notice that the features are able to detect some changes with very low error probabilities, e.g. concrete to wood (0.4%), and slate to fiberglass (0.7%). Different combinations of TAIs are expected to be useful for detecting specific material changes in the scene.

VI. DISCUSSION

The approach described above is promising in that it makes available features that are (1) invariant to scene conditions, (2) able to separate different classes of objects, and (3) based on physics based models of the many phenomena that affect LWIR image generation. We have also described a scheme for the construction of robust classifiers based on appropriate models for the distributions of the TAI features.

The specification of optimal sets of points for high inter-class separation and low intra-class variation is a crucial task in this approach. This is a complex search problem, and

(% error)	Hypothesized Material						
Actual	Wood	Slate	Dirt	Iron	Concrete	Asphalt	Fiberglass
Wood		11.7%	37.7%	45.0%	0.4%	37.5%	18.5%
Slate	6.5%		2.4%	11.5%	0.6%	16.6%	6.8%
Dirt	3.3%	20.1%		5.3%	19.5%	31.1%	0.6%
Iron	5.2%	5.2%	18.3%		16.3%	10.1%	9.3%
Concrete	5.0%	2.6%	23.7%	2.1%		19.5%	17.1%
Asphalt	3.5%	2.5%	37.8%	2.8%	19.2%		25.1%
Fiberglass	4.4%	0.7%	33.8%	25.9%	0.8%	22.0%	

TABLE V

THE TOTAL PROBABILITY OF ERROR OF A CAUCHY CLASSIFIER GIVEN A SINGLE SAMPLE VALUE. SEVERAL DIFFERENT POINT SETS WERE USED AND THE TAI WITH THE MINIMUM PROBABILITY OF ERROR WAS CHOSEN FOR EACH CELL. NOTE THAT THE DIAGONAL CORRESPONDS TO SUBSTITUTING THE CORRECT DATA VALUES BACK INTO THE HYPOTHESIZED DATA VALUES.

it is not clear that a solution will always exist for a collection of object classes. Note that different aspects of an object may be imaged – the set of visible points differ for each aspect. The complexity of the search task is compounded by attempting to ensure inter-class separation in the presence of erroneous pose hypothesis.

Some criteria for the choice of point sets are obvious. Points should not be chosen such that the measurement matrix has less than full rank. This occurs, for example, when the five points lie on surfaces with identical surface normals and also have identical thermophysical properties. When the two sets of points have four points in common, and when the remaining two points are on different parts of the imaged object, but lie on materials that are identical/similar, then these point sets will form an invariant that has a magnitude of one. Such invariants are useful only if there exists a unique set, or limited number of sets, of points that produces this value. Other thermophysical criteria for point set selection need to be investigated.

The hypothesis of object pose and identity is best achieved by employing geometric invariance techniques [1]. For example, conics may be fit to wheels which manifest high

contrast in LWIR imagery, and their parameter values may be used to compute GI's. This may be employed to generate object identity and pose that may be verified by the thermophysical invariance scheme described above. Future effort will be devoted to: the integration of the above scheme with GI's to produce a complete system, the study of the nature of scene-to-scene transformation of driving conditions, and a detailed exploration of the performance of the scheme when applied to a significant collection of objects, aspects, and scene conditions.

REFERENCES

- [1] D. Forsyth, J.L. Mundy, A. Zisserman, C. Coelho, A. Heller, C. Rothwell, "Invariant Descriptors for 3D Object Recognition and Pose", *IEEE Trans PAMI*, vol 13, no 12, Oct 1991
- [2] L. Quan, "Invariants of Six Points and Projective Reconstruction from Three Uncalibrated Images", *IEEE Trans PAMI*, vol 17, no 1, Jan 1995
- [3] A. Shashua, "Algebraic Functions for Recognition", *IEEE Trans PAMI*, vol. 17, no. 8, Aug 1995, pp. 779-789
- [4] O. Faugeras and B. Mourrain, "On the geometry and algebra of the point and line correspondences between N images", *Proc. IEEE ICCV*, Cambridge, MA, June 20-23, 1995, pp. 951-956.
- [5] T.H. Reiss, "Recognizing Planar Objects Using Invariant Image Features", *Lecture Notes in Computer Science*, 676, G. Goos and J. Hartmanis (Eds), Springer-Verlag, Berlin, 1993.
- [6] E. Rivlin and I. Weiss, "Local Invariants for Recognition", *IEEE Trans PAMI*, vol. 17, no. 3, March 1995, pp. 226-238
- [7] A. Shashua and M. Werman, "Trilinearity of three perspective views and its associated tensor", *Proc. IEEE ICCV*, Cambridge, MA, June 20-23, 1995, pp. 920-925.
- [8] D. Weinshall, "Direct Computation of Qualitative 3D Shape and Motion Invariants", *IEEE Trans PAMI*, vol 13, no 12, Dec 1991.
- [9] D. Weinshall, "Model-based Invariants for 3D Vision", *Proc IEEE CVPR 1993*, pp. 695-696
- [10] I. Weiss, "Noise-Resistant Invariants of Curves", *IEEE Trans PAMI*, vol 15, no 9, July 1993, pp. 943-948
- [11] T. Binford, T.S. Levitt, and W.B. Mann, "Bayesian Inference in Model-Based Vision", *Uncertainty in AI*, 3, L.N. Kanal, T.S. Levitt, and J.F. Lemmer, (Ed's), Elsevier, 1989.
- [12] M. Zerroug and R. Nevatia, "Quasi-Invariant Properties and 3D Shape Recovery of Non-Straight, Non-Constant Generalized Cylinders", *Proc IEEE CVPR 1993*, pp 96-103
- [13] J.B. Burns, R.S. Weiss, and E.M. Riseman, "View Variation of Point-Set and Line-Segment Features", *IEEE Trans PAMI*, vol 15, no 1, Jan 1993.
- [14] G.J. Klinker, S.A. Shafer and T. Kanade, "Image Segmentation and Reflection Analysis through Color", *Proceedings of DARPA Image Understanding Workshop*, Cambridge, MA, 1988, pp 838 - 853.
- [15] G. Healey, "Using Color to Segment Images of 3-D Scenes", *Proc SPIE Conf Applications of AI*, vol. 1468, 1988, Orlando, FL, pp. 814-825.
- [16] G. Healey and D. Slater, "Using Illumination Invariant Color Histogram Descriptors for Recognition", *Proc IEEE Conf CVPR*, June 21-24, 1994, Seattle, WA, pp. 355-360.

- [17] L.B. Wolff, "Polarization-based material classification from specular reflection", *IEEE Trans PAMI*, Nov 1990, pp 1059-1071.
- [18] S.K. Nayar and R.D. Bolle, "Reflectance Ratio: A Photometric Invariant for Object Recognition", *Proc IEEE ICCV*, 1993.
- [19] F.P. Incropera and D.P. DeWitt, *Fundamentals of Heat Transfer*, John Wiley and Sons, New York, 1981.
- [20] D. Hilbert, *Theory of Algebraic Invariants*, Cambridge University Press, transcribed in 1897, English Translation first published in 1993.
- [21] N. Nandhakumar, V.J. Velten and J.D. Michel, "Thermophysical Affine Invariants from IR Imagery for Object Recognition", *IEEE Computer Society Workshop on Physics Based Models for Computer Vision*, Cambridge, MA, June 18-20, 1995, pp. 48-54.
- [22] M.J. Gauder, V.J. Velten, L.A. Westerkamp, J. Mundy, and D. Forsyth, "Thermal Invariants for Infrared Target Recognition", *ATR Systems and Technology Conf*, 1993.
- [23] D.G. Lowe, "The Viewpoint Consistency Constraint," *International Journal of Computer Vision*, vol. 1, no. 1, 1987, pp. 57-72.
- [24] N. Nandhakumar and J.K. Aggarwal, "Integrated Analysis of Thermal and Visual Images for Scene Interpretation", *IEEE Trans. on Pattern Analysis and Machine Intelligence*, Vol. 10, No. 4, July 1988, pp. 469-481.
- [25] N. Nandhakumar and J.K. Aggarwal, "Thermal and Visual Information Fusion for Outdoor Scene Perception", *Proc. of IEEE International Conference on Robotics and Automation*, Philadelphia, PA, April 1988, pp. 1306-1308.
- [26] R. Zhang, P.-S. Tsai, J.E. Cryer, M. Shah, "Analysis of Shape from Shading Techniques", *Proc IEEE CVPR*, Seattle, WA, 1994, pp. 377-384.
- [27] N. Nandhakumar, "Robust Physics-Based Analysis of Thermal and Visual Imagery, *Journal of Optical Society of America*, JOSA-A, Special Issue on Physics-Based Computer Vision, vol 11, no 11, Nov 1994, pp. 1-9.
- [28] G.B. Gurevich, "Foundations of the Theory of Algebraic Invariants", (translated by J.R.M. Raddock and A.J.M. Spencer) P. Noordhoff Ltd - Groningen, The Netherlands, 1964
- [29] E. Barrett, G. Gheen, and P. Payton, "Algorithms for Invariant Model Transfer and Object Recognition", *Proc ARPA Image Understanding Workshop*, Monterey, CA, Nov 13-16, 1994, pp. 1429-1442.
- [30] A. Papoulis, *Probability, Random Variables, and Stochastic Processes*, McGraw-Hill, Tokyo, 1981.
- [31] C.L. Nikias and M. Shao, *Signal Processing with Alpha-Stable Distributions*, John Wiley and Sons, New York, 1995.
- [32] M. Shao and C.L. Nikias, "Signal Processing with fractional lower-order moments: Stable processes and their applications", *Proc IEEE*, vol 81, pp 986-1010, 1993
- [33] G.A. Tsihrintzis and C.L. Nikias, "Fast Estimation of the Parameters of Alpha-Stable Impulsive Interference", *IEEE Transactions on Signal Processing*, accepted for publication
- [34] G.A. Tsihrintzis and C.L. Nikias, "Performance of Optimum and Suboptimum Receivers in the Presence of Impulsive Noise Modeled as an Alpha-Stable Process", *IEEE Transactions on Communications*, vol. COM-43, pp. 904-914, 1995